Journal of Materials Chemistry C

Accepted Manuscript

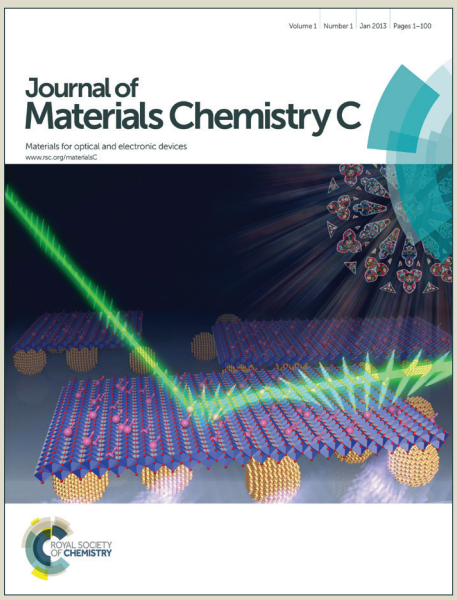

ROYAL SOCIETY OF CHEMISTRY

www.rsc.org/materialsC

Journal of Materials Chemistry C

Journal of Materials Chemistry C

Dynamic Article Links ►

Cite this: DOI: 10.1039/c0xx00000x

ARTICLE TYPE

www.rsc.org/xxxxxx

Effect of thermal annealing on the active layer morphology and performance for small molecule bulk heterojunction organic solar cells†

Zuo Yi, Wang Ni, Qian Zhang, Miaomiao Li, Bin Kan, Xiangjian Wan, Yongsheng Chen*

Received (in XXX, XXX) Xth XXXXXXXXX 20XX, Accepted Xth XXXXXXXXX 20XX

DOI: 10.1039/b000000x

New molecule design and device optimization are two main strategies to obtain high performance organic photovoltaics. In this paper, bulk heterojunction solar cell devices using a newly designed solution-processable small molecule (DRDTSBDTT) were systematically investigated for their *J-V* behavior and the morphology of active layer under different annealing treatment to understand the impact of thermal annealing on open circuit voltage, short circuit current and fill factor. A strong relationship between thermal annealing and these factors was found. *J-V* behavior analysis indicates that this is due to the efficiency change of the fundamental exciton diffusion, charge separation and collection steps, which is supported by the studies of morphology for the active layer at different thermal treatment. The results show that, for the optimized performance of a given molecule, the morphology and phase control is the most important factor to achieve the intrinsic best performance. With these, the power conversion efficiency was increased from 3.36% to 5.05% under the optimized annealing treatment for DRDTSBDTT based devices.

Introduction

Organic photovoltaics (OPVs) have attracted significant attention as an alternative solution to increasing energy problems because of their attractive features such as low-cost, lightweight, solution processability and potential use in flexible devices.[1-6] In recent years, both polymer based photovoltaics (P-OPVs) and small molecule based OPVs (SM-OPVs) have achieved power conversion efficiencies (PCEs) over 9% in single layer cells[7-10] and over 10% in tandem cells.[11,12] It is believed that SM-OPVs is a powerful competitor of P-OPVs, because SM-OPVs have several advantages such as defined structures without batch-to-batch variations, easy control of energy levels by chemical structure design and relatively simple synthesis and purification.[13-15] On the road to achieving high PCEs, new molecule design and device optimization, especially morphology control, are two main strategies that currently attract the most attention.[4,6,16-20] Similar to those used for P-OPVs, strategies such as thermal annealing have been also used during the SM-OPV device optimization by our and other groups[21-26] In this work, an investigation of the effect of thermal annealing on device performance was carried out for a new solution-processable small molecule DRDTSBDTT. The open circuit voltage (V_{oc}), short circuit current (J_{sc}) and fill factor (FF) of the devices changed regularly with the increasing of annealing temperature, and a power conversion efficiency (PCE) of 5.05% was obtained by annealing at 80 °C for 10 min. In order to understand how thermal annealing affects the devices, 1-diode Shockley equation and charge collection model was utilized to analysis the corresponding *J-V* curves, and a qualitative relationship was built between thermal annealing and diode saturation current, charge recombination, respectively. The recombination mechanism was also supported by morphology studies using grazing incidence wide-angle X-ray scattering (GI-WAXS) and transmission electron microscopy (TEM).

Experimental

Materials and synthesis

All reactions and manipulations were carried out under argon atmosphere with the use of standard Schlenk techniques. [6, 6]-Phenyl-C_{71}-butyric acid methyl ester ($PC_{71}BM$) was purchased from American Dye Source, Inc. Other starting materials were all purchased from commercial suppliers and used without further purification. 4,4'-dioctyl-5,5'-bis(trimethyltin)-dithieno-[3,2-b:2',3'-d]silole (Compound 1) and 2,6-bis(trimethyltin)-4,8-bis(5-ethylhexyl-2-thienyl)-benzo[1,2-b:4,5-b']dithiophene (compound 4) were prepared according to methods reported in the literature.[27,28] The synthesis of DRDTSBDTT is outlined in Scheme 1.

Compound 2: A Vilsmeier reagent, which was prepared with $POCl_3$ (0.95 ml, 10.4 mmol) in DMF (10 ml), was added to a cold solution of compound 1 (4.00 g, 9.55 mmol) in 1,2-dichloroethane (120 ml) at 0 °C. After stirring at 60 °C for 24 h, the mixture was poured into ice water (100 ml), neutralized with $NaHCO_3$, and then extracted with dichloromethane. The

combined organic layer was washed with water and brine and dried over Na_2SO_4. After removal of the solvent, it was chromatographed on silica gel using a mixture of dichloromethane and petroleum ether (1:1) as eluent to yield compound 2 (3.76 g, 88.2 %) as a light green liquid. ^{1}H NMR (400 MHz, $CDCl_3$): δ 9.87 (s, 1H), 7.71 (s, 1H), 7.41 (d, *J*=4.8 Hz, 1H), 7.12 (d, *J*=4.8 Hz, 1H), 1.40-1.20 (m, 28H), 0.93 (m, 6H) ppm; ^{13}C NMR (100 MHz, $CDCl_3$): δ 182.70, 158.66, 148.02, 146.32, 144.45, 142.52, 139.67, 130.09, 128.94, 33.10, 31.84, 29.16, 29.11, 24.10, 22.64, 14.11, 11.64 ppm. HRMS (ESI- FTMA) m/z: Calcd for $C_{25}H_{38}OS_2SiNa$ $[M+Na]^+$ 469.2031; found 469.2029.

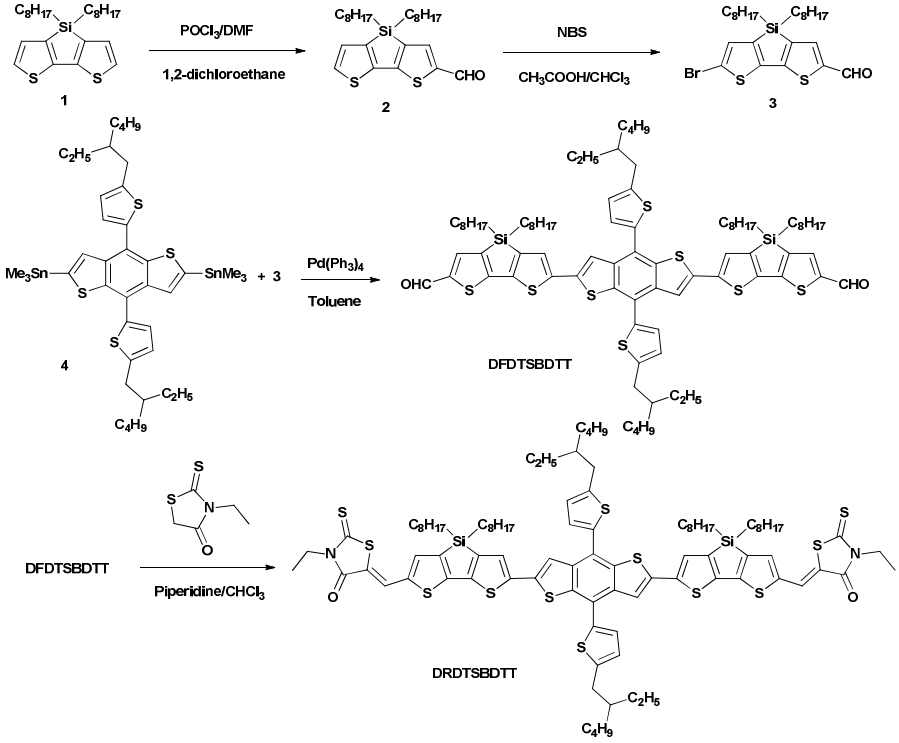

Scheme 1 synthesis route of DRDTSBDTT

Compound 3: N-Bromosuccinimide (1.57 g, 8.82 mmol) was added in small portions to a solution of compound 2 (3.76 g, 8.42 mmol) in chloroform and acetic acid (30 mL, 1:1, v/v) at 0 °C. After stirring for 4 h at room temperature, the reaction mixture was poured into water (100 ml) and extracted with CH_2Cl_2. The organic layer was thoroughly washed with water, aqueous sodium bicarbonate, brine, water, and then dried over Na_2SO_4. After removal of the solvent it was chromatographed on silica gel using a mixture of dichloromethane and petroleum ether (1:2) as eluent to yield compound 3 (3.86 g, 87.3 %) as a light green oil. ^{1}H NMR (400 MHz, $CDCl_3$): δ 9.87 (s, 1H), 7.70 (s, 1H), 7.08 (s, 1H), ^{13}C NMR (100 MHz, $CDCl_3$): δ 182.60, 157.61, 148.41, 146.60, 144.77, 141.49, 139.37, 132.72, 115.57, 33.08, 31.83, 29.16, 29.08, 24.03, 22.65, 14.11, 11.52, 1.40-1.20 (m, 28H), 0.93 (m, 6H) ppm. HRMS (ESI- FTMA) m/z: Calcd for $C_{25}H_{37}BrOS_2SiNa$ $[M+Na]^+$ 547.1136; found 547.1135.

Compound DFDTSBDTT: A solution of compound **4** (0.91 g, 1.01 mmol) and **3** (1.16 g, 2.21 mmol) in toluene (30 mL) was degassed twice with argon followed by the addition of $Pd(PPh_3)_4$ (58.0 mg, 0.0502 mmol). After stirring at 100 °C for 48 h under argon, the reaction mixture was poured into cold water and extracted with CH_2Cl_2. The organic layer was washed with water and then dried over anhydrous $MgSO_4$. After removal of the solvent, the crude product was purified by silica gel using a mixture of dichloromethane and petroleum ether (2:1) as eluent to yield compound DFDTSBDTT (1.05 g, 71.4 %) as a red solid. ^{1}H NMR (400 MHz, $CDCl_3$): δ 9.87 (s, 2H), 7.71 (s, 2H), 7.68 (s, 2H), 7.32 (d, *J*=3.4 Hz, 2H), 7.29 (s, 2H), 6.94 (d, *J*=3.4 Hz, 2H), 2.91 (q, 4H), 1.72 (m, 2H), 1.40-1.20 (m, 72H), 0.97 (m, 24H) ppm; ^{13}C NMR (100 MHz, $CDCl_3$): δ 182.58, 158.15, 147.84, 140.75, 146.23, 144.94, 142.70, 141.80, 139.53, 138.82, 137.55, 137.44, 136.62, 128.16, 127.91, 125.59, 123.51, 119.68, 41.54, 34.39, 33.18, 32.56, 31.87, 29.22, 29.12, 29.01, 25.87, 24.13, 23.13, 22.68, 14.30, 14.14, 11.64, 11.01ppm. MS (MALDI-TOF) m/z: Calcd for $C_{84}H_{114}O_2S_8Si_2$ $[M]^+$, 1466.61; found 1466.60.

Compound DRDTSBDTT: Under the protection of argon, three drops of piperidine was added to a chloroform (50 mL) solution of DFDTSBDTT (0.48 g, 3.27 mmol) and 3-ethylrhodanine (0.52 g, 3.22 mmol). The resulting solution was stirred and refluxed for 48 h. The reaction mixture was then poured into cold water and extracted with CH_2Cl_2. The organic layer was washed with water and then dried over anhydrous $MgSO_4$. After removal of the solvent, the crude product was purified by silica gel using chloroform as eluent. The crude solid was recrystallized from a mixed solvent of $CHCl_3$ and n-hexane three times to yield DRDTSBDTT as a black solid (0.49g, 85.5%). ^{1}H NMR (400 MHz, $CDCl_3$): δ 7.87 (s, 2H), 7.67 (s, 2H), 7.35 (s, 2H), 7.33 (d, *J*=3.4 Hz, 2H), 7.27 (s, 2H), 6.95 (d, *J*=3.4 Hz, 2H), 4.19 (q, 4H), 2.37 (q, 4H), 1.73 (m, 2H), 1.40-1.20 (m, 78H), 0.97 (m, 24H) ppm; ^{13}C NMR (100 MHz, $CDCl_3$): δ 190.57, 165.97, 155.73, 146.91, 145.08, 144.73, 142.97, 140.33, 138.51, 137.34, 136.20, 136.12, 135.76, 126.85, 124.44, 123.97,

122.00, 117.96, 117.67, 40.47 , 38.75, 33.35, 32.28, 31.59, 30.88, 28.70, 28.26, 28.17, 28.02, 24.78, 23.18, 22.16, 21.67, 13.33, 13.11, 11.27, 10.64, 9.97 ppm. MS (MALDI-TOF) m/z: Calcd for $C_{94}H_{124}N_2O_2S_{12}Si_2$ $[M]^+$, 1752.58; found 1752.57. Anal. Calcd for $C_{94}H_{124}N_2O_2S_{12}Si$: C, 64.33; H, 7.12; N, 1.60; found: C, 64.54; H, 7.25; N, 1.86.

Characterization

^1H and ^{13}C NMR spectra were recorded on a Bruker AV400 Spectrometer. Elemental analyses were performed using a vario EL cube elemental analyzer Matrix assisted laser desorption/ionization time-of-flight mass spectrometry (MALDI-TOF) were performed on a Bruker Autoflex III LRF200-CID instrument. Thermo gravimetric analyses (TGA) were carried out on a NETZSCH STA 409PC instrument under a purified nitrogen gas flow with a 10 °C min^{-1} heating rate. Differential scanning calorimetry (DSC) results were obtained using a DSC Q100 V9.0 Build 275 analyzer under a purified nitrogen gas flow with a 10 °C min^{-1} scanning rate. UV-vis spectra were obtained with a JASCO V-570 spectrophotometer. Cyclic voltammetry (CV) experiments were performed with a LK98B II Microcomputer-based Electrochemical Analyzer. CV measurements were carried out at room temperature with a conventional three-electrode configuration using a glassy carbon electrode as the working electrode, a saturated calomel electrode (SCE) as the reference electrode, and a Pt wire as the counter electrode. Tetrabutylammonium phosphorus hexafluoride (Bu_4NPF_6, 0.1 M) in tetrahydrofuran (THF) was used as the supporting electrolyte, and the scan rate was 100 mV s^{-1}. Highest occupied molecular orbital (HOMO) and lowest unoccupied molecular orbital (LUMO) energy levels were calculated from the onset oxidation potential and the onset reduction potential, using the equations E_{HOMO}= -(4.8+E^{ox}_{onset}), E_{LUMO}= -(4.8+E^{re}_{onset}).

Samples for the two-dimensional (2D) grazing incidence wide-angle X-ray scattering (GI-WAXS) were prepared on PEDOT: PSS-coated Si substrates using the same preparation conditions as for the devices. The data were obtained with an area CCD detector of 3072 by 3072 pixels resolution (225 mm by 225 mm) at beamline BL14B1 of the Shanghai Synchrotron Radiation Facility (SSRF). The monochromatic energy of the X-ray source was 10 keV. The X-ray wavelength was 1.2378 Å and the incidence angle was 0.15°. Transmission electron microscope (TEM) investigation was performed on a Philips Tecnai G^2 F20 operated at 200 kV. The specimen for TEM measurement was prepared by spin casting the blend solution on ITO/PEDOT: PSS substrate, then floating the film on a water surface, and transferring it to TEM grids.

Solar cell fabrication and testing

All fabrication was carried out at 30 °C. The solar cells were fabricated using a solution process with a conventional structure of glass/ITO/PEDOT: PSS/donor-acceptor/Al. The ITO-coated glass substrates were cleaned by ultrasonic treatment in detergent, deionized water, acetone, and isopropyl alcohol under ultrasonication for 15 min each and subsequently dried by blowing nitrogen. A PEDOT: PSS thin layer (around 40nm) (Clevios P VP AI 4083, filtered at 0.45 μm) was spin coated at 3000 rpm onto the ITO surface. After baking at 150°C for 20 min, the substrates were transferred to an argon-filled glovebox. Subsequently, the active layer (around 90 nm) was spin-coated from a donor-acceptor blended chloroform solution with different ratios at 1800 rpm, and then annealed at different temperatures for 10 min. Finally, an 80 nm Al layer was deposited on the active layer under high vacuum (below 2×10^{-4}Pa). A shadow mask was utilized to pattern an inland-type electrode on the active layer according to literature.[29] The effective area of each cell was around 4mm^2. The current density-voltage (J–V) curve of the photovoltaic device was obtained by a Keithley 2400 source-measure unit. The photocurrent was measured under illumination simulated 100 mW/cm^2 AM1.5G irradiation using an Oriel 96000 solar simulator, calibrated with a standard Si solar cell. External Quantum Efficiency (EQE) values of the devices were obtained using a lock-in amplifier (SR810, Stanford Research Systems). The encapsulated devices were illuminated by monochromatic light from a 150 W xenon lamp passing through an optical chopper and a monochromator. Photon flux was determined by a calibrated standard silicon photodiode.

RESULTS AND DISCUSSION

Synthesis and thermal stability

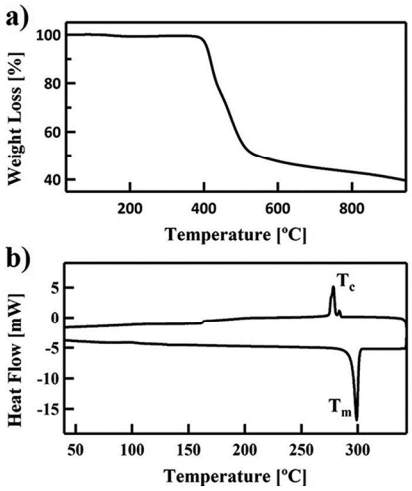

Fig. 1 Thermal property measurements of pure DRDTSBDTT powder: (a) Thermo gravimetric analyses (TGA) plot and (b) Differential scanning calorimetry (DSC) traces. Both measurements were carried out with a heating rate of 10 °C min^{-1} under a nitrogen gas flow.

Using 2-ethylhexoxy thiophene substituted benzo[1,2-b:4,5-b']dithiophene (BDTT) as the central building block, we selected dithieno[3,2-b:2',3'-d]silole (DTS) instead of the trioctylterthiophene used earlier.[30] DFDTSBDTT was obtained through Stille coupling between compund 3 and 4. The target molecule was prepared by Knoevenagel condensation of DFDTSBDTT with electron-deficient unit 3-ethylrhodanine-dye. The TGA plot shown in Fig. 1a suggests that DRDTSBDTT exhibits excellent stability with a decomposition temperature above 400 °C under a N_2 atmosphere. The DSC result shown in Fig. 1b suggested that DRDTSBDTT has a tendency to crystallize[31] because it exhibits a relatively high melting temperature (T_m) at 298.2 °C and a main isotropic-to-crystalline transition (T_c) at 278.1 °C. And DRDTSBDTT is a crystalline rather than amorphous at room temperature.[32] The reason for the small peak in DSC besides the main crystallization peak is

unclear, but it could be due to an intermediate phase.

Optical absorption and electronic properties

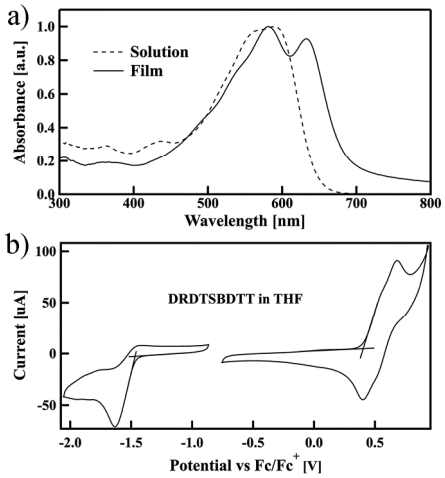

Fig. 2 Optical absorption and electronic properties of DTDTSBDTT: (a) UV-vis absorption spectra of DRDTSBDTT solution in $CHCl_3$ (dashed line) and a film on quartz substrate (solid line); (b) Cyclic voltammetry (CV) of DRDTSBDTT in THF with 0.1 Bu_4NPF_6 as supporting electrolyte and a scan speed of 100 mV/s.

UV-vis absorption spectra for DRDTSBDTT in a chloroform solution and a thin film spin-coated on a quartz substrate are shown in Fig. 2a. The DRDTSBDTT solution has an absorption peak at 589 nm with a molecular absorption coefficient of 1.2×10^5 $Lmol^{-1}cm^{-1}$. Different from solution absorption, the film spectrum shows two peaks at 582 nm and 633nm, with a maximum absorptivity of 7.0×10^3 cm^{-1}. The strong 633 nm peak could be attributed to well-ordered packing between the molecule backbones in the film state.[33] The optical band gap of DRDTSBDTT is 1.82 eV, which was estimated from the onset of its film spectrum. The energy levels of the HOMO and LUMO were calculated from CV data shown in Fig. 2b, and found to be -5.20 and -3.33 eV, respectively, with an electrochemical band gap of 1.87 eV. The LUMO level of $PC_{71}BM$ was found to be -3.81 eV under the same experimental condition (Fig. S5).

Photovoltaic performance

BHJ devices were fabricated and optimized using different donor/acceptor weight ratios of DRDTSBDTT and $PC_{71}BM$, with a general device structure of ITO/PEDOT: PSS/donor: acceptor/Al using the conventional solution spin-coating process. Different ratios of donor/acceptor fwere studied and the optimized donor/acceptor weight ratio for DRDTSBDTT is 1:1 with $PC_{71}BM$ as the acceptor, and a PCE of 3.36% was obtained. When annealed at 80 °C for 10 min, a significantly improved PCE 5.05 % was achieved, with a V_{oc} of 0.975 V, a J_{sc} of 10.08 mA/cm^2, and a FF of 51.3 %. The *J-V* curves of these devices are shown in Fig. 3 and the corresponding device performance parameters are summarized in Table 1.

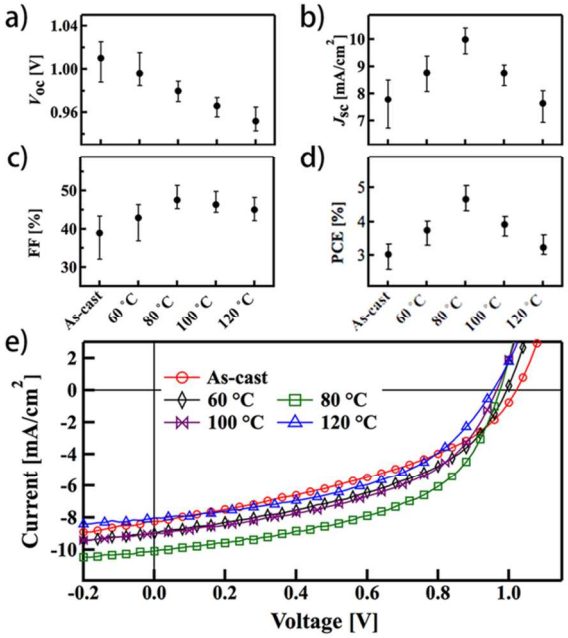

Fig. 3 Photovoltaic performance of devices prepared from DRDTSBDTT/$PC_{71}BM$ (1:1 w/w) blend annealed at different temperatures for 10 min. (a-d) Open circuit voltage (V_{oc}), short circuit current density (J_{sc}), fill factor (FF), and power conversion efficiency (PCE) for 20 cells, respectively. (e) *J-V* curves of the best device for each thermal treatment condition.

Table 1 Summary of the best device performance of DRDTSBDTT/$PC_{71}BM$ based solution processed organic solar cells annealed at different temperatures for 10 min.

D/A ratio (w/w)	Annealing Temp.	V_{oc} [V]	J_{sc} [mA/cm^2]	FF [%]	PCE [%]
1:0.5	None	1.008	6.61	28.7	1.91
1:0.8	None	1.021	7.32	39.2	2.93
1:1.0	None	1.022	8.25	39.9	3.36
1:1.2	None	0.975	6.65	41.9	2.72
1:1.0	60 °C	0.994	8.99	44.8	4.00
1:1.0	80 °C	0.975	10.08	51.3	5.05
1:1.0	100 °C	0.966	8.96	48.2	4.17
1:1.0	120 °C	0.956	8.02	47.4	3.63

From Table 1, there are two obvious trends with an increase of annealing temperature: (1) the V_{oc} of the hero device drops step-by-step from 1.022 to 0.956 V, and (2) J_{sc} and FF both increase initially and then decrease, reaching their maximum values at an annealing temperature of 80 °C.

Effect of thermal annealing on V_{oc}

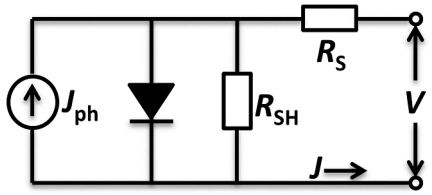

Fig. 4 1-diode equivalent circuit mode commonly employed in describing the *J-V* behavior of OPV devices

In order to investigate how thermal annealing affected the V_{oc}, *J-V* curves from the best devices, prepared with a DRDTSBDTT/$PC_{71}BM$ (1:1 w/w) blend at different annealing

temperatures, has been studied.

The *J-V* behaviour could mostly be described by 1-diode Shockley equation[34-38]:

$$J(V) = J_0\{\exp[\frac{q(V-R_SJ)}{nk_BT}] - 1\} + \frac{V-R_SJ}{R_{SH}} - J_{ph}(V) \quad (1)$$

In eqn (1), J is the cell output current, V is the applied voltage across the cell terminals, J_0 is the reverse saturation current, T is the absolute temperature, q is the absolute value of electron charge, k_B is Boltzmann's constant, n is the ideality factor, R_S is the cell series resistance and R_{SH} is the cell shunt resistance. $J_{ph}(V)$ is the voltage-dependent photocurrent density.[34,39] The equivalent circuit mode is present in Fig. 4.

Under open circuit conditions ($V = V_{oc}$), there is no output current ($J = 0$) because all the photo-generated current is forced to combine. Assuming the series resistance is low, eqn (1) could be simplified and we obtain the equation for V_{oc}:[34]

$$V_{oc} = \frac{nk_BT}{q}\ln[\frac{J_{ph}(V_{oc})}{J_0} + 1] \approx \frac{nk_BT}{q}\ln[\frac{J_{ph}(V_{oc})}{J_0}] \quad (2)$$

In eqn (2), $J_{ph}(V_{oc})$ is the photo-generated current density at V=V_{oc}, which is equal to the dark current density at V_{oc}. The $J_{ph}(V_{oc})$ data with different annealing condition were presented in Table 2.

Under dark conditions, the $J_{ph}(V)$ = 0, and eqn (1) can be written as below:

$$J(V) = J_0\{\exp[\frac{q(V-R_SJ)}{nk_BT}] - 1\} + \frac{V-R_SJ}{R_{SH}} \quad (3)$$

J-V dark data of the best devices with different annealing temperatures were fitted by eqn (3). The corresponding fitting curves are presented in Fig. 5a and the fitted values of J_0 and n are summarized in Table 2. Using the values of J_0, n and $J_{ph}(V_{oc})$ with eqn (2), the simulated open circuit voltage ($V_{oc,cal}$) can be obtained. As we can see from Fig. 5b, the simulated values of $V_{oc,cal}$ are consistent in trend with the experimental V_{oc} results.

From eqn (2), we can see that with the increase of annealing temperature, both n and J_0 increase. But since n and J_0 have opposite effects on V_{oc} as shown in eqn (2), the decreasing trends of the observed and calculated V_{oc} indicate that J_0 plays a bigger role in changing V_{oc}. So with increasing annealing temperature, the increase of J_0 causes the open voltage to decrease. Similar result has been obtained by previous studies.[39-42]

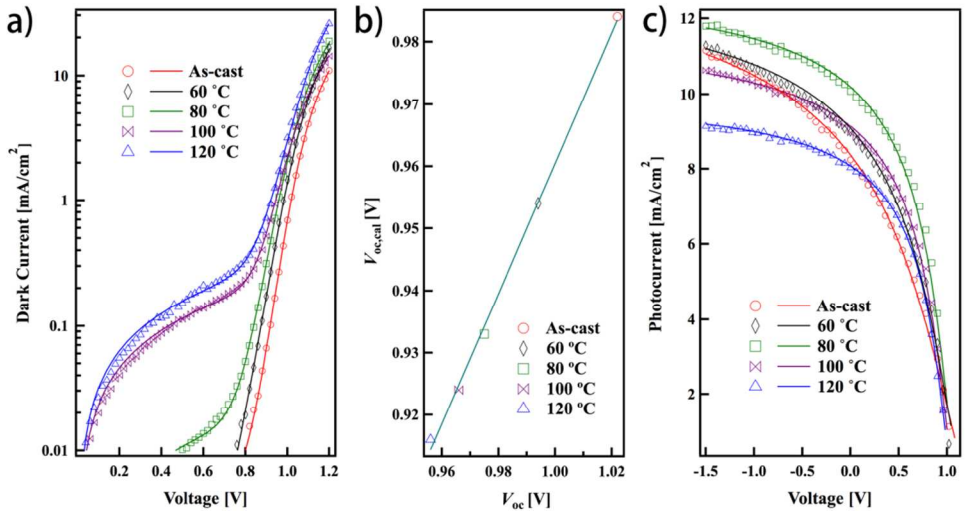

Fig. 5 Current-voltage characteristics measured from the best devices prepared from a DRDTSBDTT/$PC_{71}BM$ (1:1 w/w) blend annealed at different temperatures for 10min. (a) Output dark current versus applied voltage. Points are the experimental data and the solid lines are fits using eqn (3). (b) Correlation between the experimental open circuit voltage (V_{oc}) and simulated open circuit voltage ($V_{oc,cal}$). (c) Steady state photocurrent density versus voltage characteristics. Points are the experimental data and the solid lines are fits using (4).

Table 2. Summary of extracted parameters fitted by the *J-V* and J_{ph}-*V* curves from the best devices, prepared using a DRDTSBDTT/$PC_{71}BM$ (1:1 w/w) blend with different annealing temperatures. n, J_0 come from eqn (3), and $J_{ph,sat}$, S come from eqn (4). $V_{oc,cal}$ is the simulated voltage calculated from eqn (2), while V_{oc} is the experimental value of the corresponding cell.

Annealing Temp.	n	J_0 [mA/cm²]	$J_{ph}(V_{oc})$ [mA/cm²]	$V_{oc,cal}$ [V]	V_{oc} [V]	$J_{ph,sat}$ [mA/cm²]	$J_{sc}/J_{ph,sat}$	S
None	1.50	1.47×10^{-11}	1.11	0.984	1.022	14.04	58.7%	0.76
60 °C	1.71	7.10×10^{-10}	1.31	0.954	0.994	13.25	67.8%	1.10
80 °C	1.78	2.59×10^{-9}	1.40	0.933	0.975	13.05	77.2%	1.81
100 °C	1.90	1.11×10^{-8}	1.41	0.924	0.966	11.74	76.4%	1.82
120 °C	2.10	9.10×10^{-8}	1.57	0.916	0.956	10.09	79.5%	2.09

Effect of thermal annealing on J_{sc} and FF

The voltage-dependent photocurrent density $J_{ph}(V)$ can be analysed by a charge collection model, which is shown below:[43]

$$J_{ph}(V) = J_{ph,sat}(V_{BI} - V)S\left[1 - \exp\left(-\frac{1}{(V_{BI}-V)S}\right)\right]; S = \mu\tau/dd' \quad (4)$$

Where $J_{ph,sat}$ is the current at full charge collection which is expected to occur at sufficiently large reverse bias, V_{BI} is the built-in potential, V is the applied voltage across the cell terminals, S is the charge collection parameter which is associated with the mobility-lifetime product $\mu\tau$, sample thickness d and average carrier travel distance d' (~d/2), and $J_{ph}(V)$ is considered to be the difference between the current under illumination and in the dark. By fitting the experimental J_{ph}-V data with eqn (4), values of $J_{ph,sat}$ and S are obtained. The corresponding fitting curves are presented in Fig. 5c and the fitted values of $J_{ph,sat}$ and S are summarized in Table 2

The photocurrent density $J_{ph}(V)$ in eqn (4) could also be expressed as below:[43,44]

$$J_{ph}(V) = G\eta_A\eta_{ED}\eta_{CT}\eta_{CC}(V) \quad (5)$$

Here, V is the applied voltage across the cell terminals, G is the incident light intensity, η_A is the absorption efficiency of the photons in the active layer, η_{ED} is the exciton diffusion efficiency which is the efficiency for the photo-induced excitons to diffuse to the donor/acceptor interface, η_{CT} is the charge transfer efficiency which is related to LUMO offset between donor and acceptor, and $\eta_{CC}(V)$ is the charge collection efficiency, i.e. the probability of charge collection of the separated carriers. The charge collection efficiency (η_{CC}) is voltage-dependent.[34]

On the one hand, at a sufficiently large reverse bias, J_{ph} = $J_{ph,sat}$, and η_{CC} should approaches 100%. Hence, eqn (5) can be rewritten as below:

$$\eta_{ED}\eta_{CT} = J_{ph,sat}/(G\eta_A) \quad (6)$$

η_A was estimated by UV-vis spectrum of donor/acceptor blend films presented in Fig. 6a. By employing standard tables for reference solar spectral irradiances (ASTM G173-03 Reference Spectra Derived from SMARTS v.2.9.2 (NREL Reference Data)), the absorbed photons were calculated to be 6.04×10^{20}, 6.23×10^{20}, 6.46×10^{20} $s^{-1}m^{-2}$ at the conditions of as-cast, 80 °C and 120 °C annealed, respectively. η_A slightly increased with increasing annealing temperatures. Since all the solar cell devices were tested under the same conditions with the same incident light intensity G, and $J_{ph,sat}$ decreased when the device was annealed at a higher temperature (Table 2), it can be concluded from eqn (6) that $\eta_{ED}\eta_{CT}$ decreases when annealing temperature increases. This indicates that a growing proportion of excitons recombined by the Coulomb attraction between the geminate electron-hole pair,[45] which is harmful to J_{sc} and FF.[46] The large LUMO difference of DRDTSBDTT and $PC_{71}BM$ (0.48 eV vs 0.3 eV) should ensure the efficient exciton dissociation.[47,48] So the decreasing of η_{ED} should be the main reason for the increasing of geminated recombination, which means that a growing number of excitions recombined before they reached the donor/acceptor interface after annealing at a higher temperature.

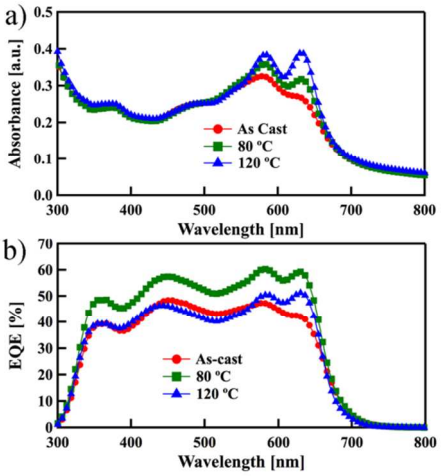

Fig. 6 Effect of thermal annealing on the absorption of the active layer and calculated current of the corresponding cells. (a) UV-vis absorption spectra of a DRDTSBDTT/PC71BM (1:1 w/w) blend film on a quartz substrate with annealed at different temperatures for 10min. (b) External quantum efficiency (EQE) spectra of the best donor/acceptor ratio device (1:1 w/w) for different thermal treatment conditions.

On the other hand, by inserting eqn (6) into eqn (5), we obtain the equation for $\eta_{CC}(V)$:[43]

$$\eta_{CC}(V) = J_{ph}(V)/J_{ph,sat} \quad (7)$$

Under short circuit condition, $\eta_{CC}(0)$ is equal to $J_{sc}/J_{ph,sat}$. $\eta_{CC}(0)$ is the charge collection efficiency at the short circuit condition, and could be a parameter to describe the charge collection process of a certain device. From $J_{sc}/J_{ph,sat}$ values presented in Table 2, it can be concluded that increasing annealing temperature increases the charge collection efficiency, but the increase is rapid at low annealing temperatures and becomes slow at higher one. This trend is consistent with the trend of the charge collection parameter S, which is an extracted parameter from eqn (4) and summarized in Table 2, too. All these factors indicate that, overall, thermal annealing is beneficial for charge collection, which should result from the lower non-geminate recombination occurs, and thus give a higher J_{sc} and FF.[46]

Above all, the combined impact of increased geminate recombination and decreased non-geminate recombination causes J_{sc} and FF to first increase then decrease with an increase of annealing temperature. These tendencies are confirmed by the EQE measurement shown in Fig. 6b, with a calculated J_{sc} of 8.01, 9.90, 8.10 mA/cm^2 at the conditions of as-cast, and 80 °C and 120 °C annealed, respectively, which is within 3% of the measured J_{sc} values.

Effect of thermal annealing on film morphology

The difference in recombination mechanisms under different thermal annealing conditions may originate from different morphology structures, and the morphology structures of DR3TBDTT/$PC_{71}BM$ blends of as-cast, and 80 °C and 120 °C annealed were characterized by grazing incidence wide-angle x-ray scattering (GI-WAXS) and transmission electron microscopy (TEM).

GI-WAXS has been widely used in describing crystallization behaviour of the active layer for its ability in measuring ultra-thin

film samples.[49-51] In this measurement, PEDOT: PSS and an active layer were spin-coated on a Si substrate, the same as in the actual OPV devices. From the 2-D diffractograms and the line-cut intensity of the out-of-plane direction shown in Fig. 7a-d, it can be found that there is no obvious diffraction peak in the as-cast thin film, while the 80 °C annealed blend showed (100) and (200) peaks. For the film annealed at 120 °C, weak (300) and (010) peaks appear, indicating that DRDTSBDTT exhibits a stronger crystallization behaviour at the higher annealing temperature. The (100) peak position and full width at half maximum (FWHM) of the 80 °C and 120 °C annealed blends were extracted by Gauss fitting. We did not have information about the as-cast film, as it shows no obvious peak. It can be seen that the DR3TBDTT has an interplanar (100) spacing of ~0.31 $Å^{-1}$, corresponding to a ~2 nm spacing. The (100) spacing slightly increases at higher annealing temperatures, which may result from the rearrangement of alkylthiophene side chains. The crystal size was estimated by the Scherrer equation from FWHM, which gave values of 20.9 and 28.5 nm, for the 80 °C and 120 °C annealed films, respectively. This indicates that the crystal size of DR3TBDTT grows with the increase of annealing temperature.

The TEM gives a clearer picture for the phase separation information about these films at different temperatures as shown in Fig. 7e-g. The dark regions in the TEM images can be attributed to PCBM domains due to its relatively high electron scattering density and the light regions refer to the donor domains.[52] From Fig. 7e-g, the as-cast film did not show any noticeable feature, indicating that good mixing occurred in the film without any clear phase separation. Meanwhile, the film heated at 80 °C exhibited a much better interpenetrating network, and the phase separation was the length scale around 20 nm. That was a good result because the ideal domains for BDT and DTS based SM-OPV materials range from 15-30 nm.[30,53-55] When the annealing temperature increased to 120 °C, a distinct phase separation could be observed in the active layer, with a domain width of 40–50 nm.

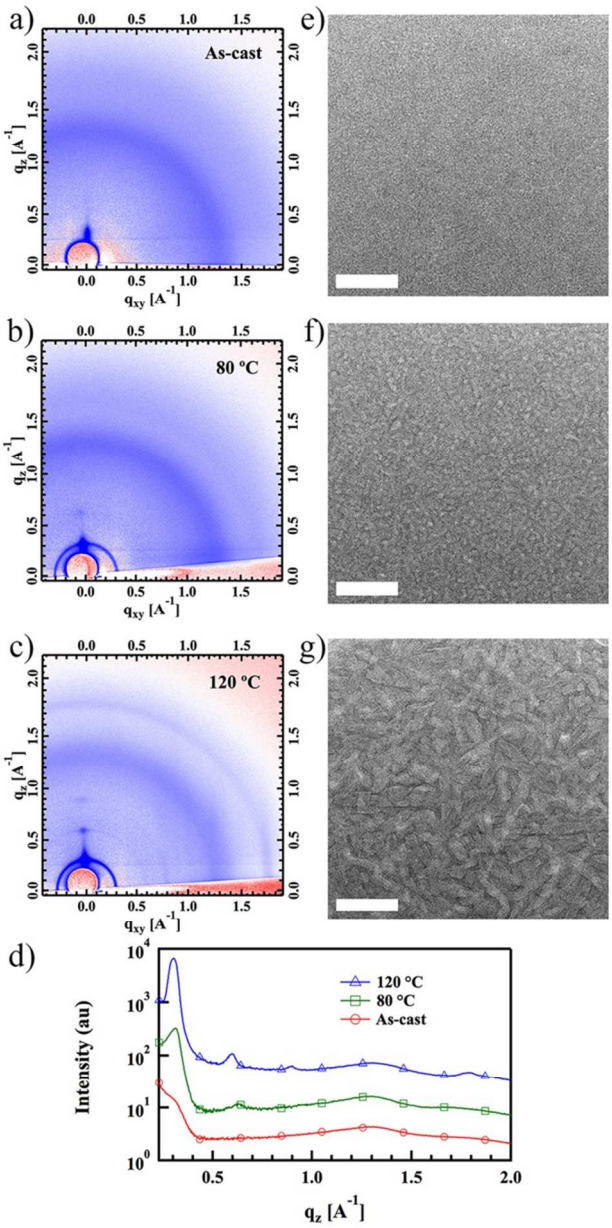

Fig. 7 Morphology structure of DR3TBDTT /$PC_{71}BM$ (1:1 w/w) blend films. Grazing incidence wide-angle x-ray scattering (GI-WAXS) patterns of (a) as-cast, (b) annealed at 80 °C, (c) 120 °C for 10 min, and (d) the line-cut intensity of the out-of plane direction. Transmission electron microscope (TEM) images of (e) as-cast, (f) annealed at 80 °C and (g) 120 °C for 10 min with scale bars of 200 nm.

All the morphology structural information is summarized in Table 3. When the active film was annealed at higher temperatures, the GI-WAXS and TEM measurements confirm that both the crystal size and phase separation became larger, and a better interpenetrating network was also formed. This trend is expected to have a bad effect on the exciton diffusion to the donor/acceptor interface, but is good for separated free charge to transport to the electrode.

Table 3 Summary of the GI-WAXS and TEM data. The samples were prepared with a (1:1 w/w) donor/acceptor ratio with different thermal conditions. The crystal size was estimated by the Scherrer equation from the FWHM, and the domain size is from statistical analysis of the TEM image

Annealing Temp.	q(100) [Å^{-1}]	d(100) [Å]	FWHM [Å]	Crystal size [Å]	Domain size [nm]
None		No obvious peaks			< 5
80 °C	0.319	19.7	0.0300	209	15-20
120 °C	0.302	20.8	0.0220	285	40-50

Conclusions

We have designed and synthesized a solution-processable linear small molecule DRDTSBDTT. Devices based on DRDTSBDTT after annealing at different temperatures have been thoroughly investigated. The best PCE of 5.05% was achieved with 80 °C annealing. From *J-V* curve analysis, it is concluded that increasing the annealing temperature increases the saturation dark current and reduces the V_{oc}. Meanwhile, supported by morphology studies, we found that as the annealing temperature increases, the film's crystal size and phase size became larger and resulted in a bigger geminate recombination. On the other hand, the higher crystallinity, larger phase separation and better interpenetrating network caused by annealing reduce the non-geminate recombination. These two opposing effects cause J_{sc} and FF to first increase then decrease. These qualitative relationships reported here not only give a clearer picture of the effect of thermal annealing on small molecule bulk heterojuction solar cells, but also will be rather useful in the device optimization process for higher OPV performance.

Acknowledgement

The authors gratefully acknowledge the financial support from MoST (Grants 2014CB643502 and 2012CB933401), NSFC (Grants51373078, 21374050 and 51273093), PCSIRT (IRT1257), NSF of Tianjin city (13RCGFGX01121) and thank beamline BL14B1 (Shanghai Synchrotron Radiation Facility) for providing beam time.

Notes and references

Key Laboratory of Functional Polymer Materials, Collaborative Innovation Center of Chemical Science and Engineering (Tianjin), Center for Nanoscale Science and Technology, Institute of Polymer Chemistry, College of Chemistry, Nankai University, Tianjin 300071, China. Fax: +86 (22) 2349-9992; Tel: +86 (22) 2350-0693; E-mail: yschen99@nankai.edu.cn

† Electronic Supplementary Information (ESI) available: ^{1}H NMR, ^{13}C NMR, MS (MALDI-TOF) spectra of DRDTSBDTT; Cyclic voltammetry of $PC_{71}BM$. See DOI: 10.1039/b000000x/

1. B. C. Thompson and J. M. Frechet, *Angew. Chem. Int. Ed.*, 2008, **47**, 58-77.
2. F. C. Krebs, J. Fyenbo and M. Jørgensen, *J. Mater. Chem.*, 2010, **20**, 8994-9001.
3. A. Mishra and P. Bauerle, *Angew. Chem. Int. Ed.* , 2012, **51**, 2020-2067.
4. Y. Lin, Y. Li and X. Zhan, *Chem. Soc. Rev.*, 2012, **41**, 4245-4272.
5. H. Wu, B. Zhao, Z. He, M. Yun, M. Wang, X. Huang, J. Wu and Y. Cao, *J. Mater. Chem. C*, 2014, DOI: 10.1039/c3tc32520b.
6. J. Roncali, *Acc. Chem. Res.*, 2009, **42**, 1719-1730.
7. Z. He, C. Zhong, S. Su, M. Xu, H. Wu and Y. Cao, *Nat. Photon.*, 2012, **6**, 593-597.
8. S. Liu, K. Zhang, J. Lu, J. Zhang, H. L. Yip, F. Huang and Y. Cao, *J. Am. Chem. Soc.*, 2013, **135**, 15326-15329.
9. S. H. Liao, H. J. Jhuo, Y. S. Cheng and S. A. Chen, *Adv. Mater.*, 2013, **25**, 4766-4771.
10. V. Gupta, A. K. Kyaw, D. H. Wang, S. Chand, G. C. Bazan and A. J. Heeger, *Sci. Rep.*, 2013, **3**, 1965.
11. J. You, L. Dou, K. Yoshimura, T. Kato, K. Ohya, T. Moriarty, K. Emery, C. C. Chen, J. Gao, G. Li and Y. Yang, *Nat. Commun.*, 2013, **4**, 1446.
12. Y. Liu, C. C. Chen, Z. Hong, J. Gao, Y. M. Yang, H. Zhou, L. Dou, G. Li and Y. Yang, *Sci. Rep.*, 2013, **3**, 3356.
13. S. Loser, C. J. Bruns, H. Miyauchi, R. P. Ortiz, A. Facchetti, S. I. Stupp and T. J. Marks, *J. Am. Chem. Soc.*, 2011, **133**, 8142-8145.
14. A. K. Kyaw, D. H. Wang, D. Wynands, J. Zhang, T. Q. Nguyen, G. C. Bazan and A. J. Heeger, *Nano Lett.*, 2013, **13**, 3796-3801.
15. J. Roncali, P. Leriche and P. Blanchard, *Adv. Mater.*, 2014, DOI: 10.1002/adma.201305999.
16. Y. Li, *Acc. Chem. Res.*, 2012, **45**, 723-733.
17. Y. Chen, X. Wan and G. Long, *Acc. Chem. Res.*, 2013, **46**, 2645-2655.
18. J. E. Coughlin, Z. B. Henson, G. C. Welch and G. C. Bazan, *Acc. Chem. Res.*, 2013, **47**, 257-270.
19. L. Ye, S. Zhang, L. Huo, M. Zhang and J. Hou, *Acc. Chem. Res.*, 2014, **47**, 1595-1603.
20. M. T. Dang and J. D. Wuest, *Chem. Soc. Rev.*, 2013, **42**, 9105-9126.
21. W. L. Leong, G. C. Welch, J. Seifter, J. H. Seo, G. C. Bazan and A. J. Heeger, *Adv. Energy Mater.*, 2013, **3**, 356-363.
22. G. C. Welch, L. A. Perez, C. V. Hoven, Y. Zhang, X.-D. Dang, A. Sharenko, M. F. Toney, E. J. Kramer, T.-Q. Nguyen and G. C. Bazan, *J. Mater. Chem.*, 2011, **21**, 12700-12709.
23. X. Wan, Y. Liu, F. Wang, J. Zhou, G. Long and Y. Chen, *Org. Electron.*, 2013, **14**, 1562-1569.
24. B. Walker, A. B. Tamayo, X. D. Dang, P. Zalar, J. H. Seo, A. Garcia, M. Tantiwiwat and T. Q. Nguyen, *Adv. Funct. Mater.*, 2009, **19**, 3063-3069.
25. Y. Lin, P. Cheng, Y. Li and X. Zhan, *Chem. Commun.*, 2012, **48**, 4773-4775.
26. W. Yong, M. Zhang, X. Xin, Z. Li, Y. Wu, X. Guo, Z. Yang and J. Hou, *J. Mater. Chem. A*, 2013, **1**, 14214-14210.
27. G. Lu, H. Usta, C. Risko, L. Wang, A. Facchetti, M. A. Ratner and T. J. Marks, *J. Am. Chem. Soc.*, 2008, **130**, 7670-7685.
28. J. Yuan, X. Huang, F. Zhang, J. Lu, Z. Zhai, C. Di, Z. Jiang and W. Ma, *J. Mater. Chem.*, 2012, **22**, 22734-22742.
29. M.-S. Kim, M.-G. Kang, L. J. Guo and J. Kim, *Appl. Phys. Lett.*, 2008, **92**, 133301.
30. J. Zhou, Y. Zuo, X. Wan, G. Long, Q. Zhang, W. Ni, Y. Liu, Z. Li, G. He, C. Li, B. Kan, M. Li and Y. Chen, *J. Am. Chem. Soc.*, 2013, **135**, 8484-8487.
31. P. Dutta, J. Kim, S. H. Eom, W. H. Lee, I. N. Kang and S. H. Lee, *ACS applied materials and interfaces*, 2012, **4**, 6669-6675.
32. H. Wang, T. Fukumatsu, Y. Liu, W. Hu, S. Seki and X. Zhan, *J. Mater. Chem. C*, 2013, **1**, 414-417.
33. T. Erb, U. Zhokhavets, G. Gobsch, S. Raleva, B. Stühn, P. Schilinsky, C. Waldauf and C. J. Brabec, *Adv. Funct. Mater.*, 2005, **15**, 1193-1196.
34. J. H. Lee, S. Cho, A. Roy, H.-T. Jung and A. J. Heeger, *Appl. Phys. Lett.*, 2010, **96**, 163303.
35. J. Appelbaum and A. Peled, *Sol. Energy Mater. Sol. Cells*, 2014, **122**, 164-173.
36. S. S. Hegedus and W. N. Shafarman, *Prog. Photovolt: Res. Appl.*, 2004, **12**, 155-176.
37. Z. Jehl-Li-Kao, T. Kobayashi and T. Nakada, *Sol. Energy Mater. Sol. Cells*, 2013, **119**, 144-148.
38. C. W. Schlenker and M. E. Thompson, *Chem. Commun.*, 2011, **47**, 3702-3716.
39. B. Rand, D. Burk and S. Forrest, *Phy. Rev. B*, 2007, **75**, 115327.
40. K. Vandewal, K. Tvingstedt, A. Gadisa, O. Inganäs and J. V. Manca, *Nat. mater.*, 2009, **8**, 904-909.

41. L. Yang, H. Zhou and W. You, *J. Phy. Chem. C*, 2010, **114**, 16793-16800.
42. G. Long, X. Wan, B. Kan, Y. Liu, G. He, Z. Li, Y. Zhang, Y. Zhang, Q. Zhang, M. Zhang and Y. Chen, *Adv. Energy Mater.*, 2013, **3**, 639-646.
43. R. A. Street, A. Krakaris and S. R. Cowan, *Adv. Funct. Mater.*, 2012, **22**, 4608-4619.
44. Z. He, C. Zhong, X. Huang, W.-Y. Wong, H. Wu, L. Chen, S. Su and Y. Cao, *Adv. Mater.*, 2011, **23**, 4636-4643.
45. C. M. Proctor, M. Kuik and T.-Q. Nguyen, *Prog. Polym. Sci.*, 2013, **38**, 1941-1960.
46. S. R. Cowan, N. Banerji, W. L. Leong and A. J. Heeger, *Adv. Funct. Mater.*, 2012, **22**, 1116-1128.
47. M. C. Scharber, D. Mühlbacher, M. Koppe, P. Denk, C. Waldauf, A. J. Heeger and C. J. Brabec, *Adv. Mater.*, 2006, **18**, 789-794.
48. H. Bai, Y. Wang, c. pei, Y. Li, D. Zhu and X. Zhan, *ACS applied materials and interfaces*, 2014, DOI: 10.1021/am501316y.
49. J. Rivnay, S. C. Mannsfeld, C. E. Miller, A. Salleo and M. F. Toney, *Chem. Rev.*, 2012, **112**, 5488-5519.
50. W. Chen, M. P. Nikiforov and S. B. Darling, *Energy Environ. Sci.*, 2012, **5**, 8045-8074.
51. F. Liu, Y. Gu, X. Shen, S. Ferdous, H. W. Wang and T. P. Russell, *Prog. Polym. Sci.*, 2013, **38**, 1990-2052.
52. X. Yang, J. Loos, S. C. Veenstra, W. J. Verhees, M. M. Wienk, J. M. Kroon, M. A. Michels and R. A. Janssen, *Nano Lett.*, 2005, **5**, 579-583.
53. Y. Sun, G. C. Welch, W. L. Leong, C. J. Takacs, G. C. Bazan and A. J. Heeger, *Nat. mater.*, 2011, **11**, 44-48.
54. C. J. Takacs, Y. Sun, G. C. Welch, L. A. Perez, X. Liu, W. Wen, G. C. Bazan and A. J. Heeger, *J. Am. Chem. Soc.*, 2012, **134**, 16597-16606.
55. J. A. Love, I. Nagao, Y. Huang, M. Kuik, V. Gupta, C. J. Takacs, J. E. Coughlin, L. Qi, T. S. van der Poll, E. J. Kramer, A. J. Heeger, T. Q. Nguyen and G. C. Bazan, *J. Am. Chem. Soc.*, 2014, **136**, 3597-3606.

Effect of thermal annealing on the active layer morphology and performance for small molecule bulk heterojunction organic solar cells

*Zuo Yi, Wang Ni, Qian Zhang, Miaomiao Li, Bin Kan, Xiangjian Wan, Yongsheng Chen**

Key Laboratory of Functional Polymer Materials, Collaborative Innovation Center of Chemical Science and Engineering (Tianjin), Center for Nanoscale Science and Technology, Institute of Polymer Chemistry, College of Chemistry, Nankai University, Tianjin 300071, China

Corresponding author:

*Prof. Yongsheng Chen.

Tel.: +86 (22) 2350-0693;

Fax: +86 (22) 2349-9992;

E-mail address: yschen99@nankai.edu.cn

Table of Contents

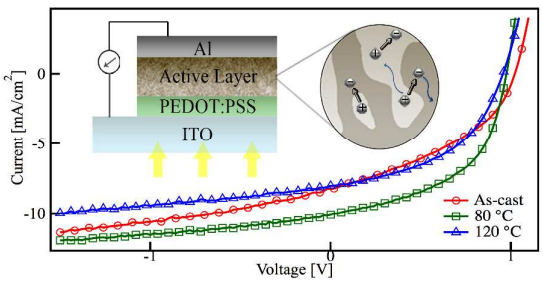

Bulk heterojunction solar cells based on a novel small molecule (DRDTSBDTT) were systematically investigated to understand the impact of thermal annealing on V_{oc}, J_{sc} and FF.